

Anisotropic spin dynamics in semiconductor narrow wires from the interplay between spin-orbit interaction and planar magnetic field

Junpei Sonehara,^{1,*} Michael Kammermeier,^{2,3,*} Dai Sato,^{1,*} Daisuke Iizasa,¹ Ulrich Zülicke[Ⓞ],² Shutaro Karube,^{1,4} Junsaku Nitta,^{1,3,4} and Makoto Kohda[Ⓞ]^{1,3,4,5,†}

¹*Department of Materials Science, Tohoku University, Sendai 980-8579, Japan*

²*School of Chemical and Physical Sciences and MacDiarmid Institute for Advanced Materials and Nanotechnology, Victoria University of Wellington, P.O. Box 600, Wellington 6140, New Zealand*

³*Center for Science and Innovation in Spintronics (Core Research Cluster), Tohoku University, Sendai 980-8577, Japan*

⁴*Center for Spintronics Research Network, Tohoku University, Sendai 980-8577, Japan*

⁵*Division for the Establishment of Frontier Sciences of the Organization for Advanced Studies, Tohoku University, Sendai 980-8577, Japan*



(Received 7 December 2021; revised 8 March 2022; accepted 9 March 2022; published 25 March 2022)

The anisotropic spin dynamics in wires based on a [001]-oriented semiconductor quantum well were investigated to determine the effect of applying an in-plane magnetic field both parallel to and perpendicular to the spin-orbit magnetic field, and the interaction between them. In one-dimensional spin motion where the wire width is less than the spin-precession length, it is known that the global spin precession is essentially determined by the spin-orbit induced precession along the wire direction. In this study, our objective is to investigate the nature of anisotropic spin dynamics in such narrow semiconductor wires along various crystal orientations. We proposed an analytic expression for the anisotropic spin-relaxation rates and the Larmor-precession frequencies for the arbitrary magnetic field orientation based on a theoretical understanding of the spin dynamics in the narrow wire structure. This expression describes the interaction between the spin-orbit field and all orientations of the in-plane magnetic field. We experimentally investigated the spin dynamics for lithographically defined 800-nm-width wires oriented along the $\bar{1}10$, [100], and [110] crystal orientations using a [001] GaAs/AlGaAs quantum well. Time-resolved Kerr rotation microscopy measurements indicated that the spin-relaxation time was the longest for the in-plane magnetic field perpendicular to the spin-orbit field, whereas the parallel configuration was found to be the shortest among all the directions. The precession frequency was found to have the opposite symmetry. These relations are well explained by the theoretical considerations developed in this work. Because the Rashba and Dresselhaus spin-orbit fields are mutually orthogonal in the [100] crystal orientation, it is possible to evaluate both spin-orbit coefficients from the precession anisotropy. These findings suggest that it is possible to control the spin state in narrow wires approaching the one-dimensional state and evaluate the spin-orbit coefficient. This has the potential to provide a greater understanding of quantum and topological information in semiconductor one-dimensional wires.

DOI: [10.1103/PhysRevB.105.094434](https://doi.org/10.1103/PhysRevB.105.094434)

I. INTRODUCTION

Spin dynamics in semiconductor low-dimensional systems play a crucially important role in that they provide the platform for various spin-related physics and devices, including spin generation [1] and detection [2], helical spin texture [3–7], nuclear spin order [8], Majorana quasiparticles [9,10], parafermion [11], and Tomonaga-Luttinger liquids [12–15]. Spin relaxation in III-V semiconductors is governed by a spin-orbit (SO) interaction which acts as a momentum-dependent effective magnetic field for moving electrons [16]. Notably, quantum confinement in one-dimensional (1D) wires restricts electrons moving along the wire direction, thereby producing a unidirectional SO field which suppresses the randomization of the spin-precession axis. The advantage of such a

well-defined SO field is that it allows the SO-induced gap towards Majorana fermions to be realized [17,18] and suppresses D'yakonov-Perel' (DP) spin relaxation [19–22]. The effects of lateral confinement on the spin dynamics have been studied intensively in spatially homogeneous spin orientation [23–25] and spatially rotated spin structures [26–28], respectively referred to as homogeneous and helical spin textures. The spin-relaxation time in both spin textures is enhanced when the lateral confinement is less than the spin-precession length [23,27], i.e., in a 1D diffusive approximation for spin, which is the definition of “narrow” wires in this context. Depending on the crystal orientation, the spin-relaxation time in such narrow wire becomes anisotropic because of the parallel and antiparallel interactions between the Rashba and Dresselhaus SO fields [24,25].

For precise control of the spin state, the relative directions of the Rashba and Dresselhaus SO fields are important. Their interaction with the external magnetic field is also crucially important. The in-plane magnetic field orientation in the 1D

*These authors contributed equally to this work.

†Corresponding author: makoto@material.tohoku.ac.jp

wires affects the spin dynamics, including spin relaxation and the Larmor precession. The focus of most of the studies examining the interaction between the SO and external magnetic field directions has been on two-dimensional (2D) electron motion in III-V semiconductor quantum wells (QWs). Therefore, the spin dynamics induced by SO and the external fields are averaged due to the random 2D electron motion [29,30]. These averaged values obscure the fundamentally important contribution to the spin relaxation and Larmor-precession frequency made by the SO and an in-plane external magnetic fields in isolation and the interaction between them. To date, no comprehensive investigation of spin dynamics has been conducted from both theoretical and experimental perspectives considering spin relaxation and the Larmor precession in narrow wire structures.

Herein, we investigate anisotropic spin dynamics in narrow wire structures based on (001)-oriented III-V semiconductor QWs under various in-plane magnetic field directions. The wire orientation is aligned along the $[\bar{1}10]$, $[100]$, and $[110]$ crystal orientations, where the relative contribution between the Rashba and Dresselhaus SO fields becomes anisotropic. First, we establish a theoretical framework for the time evolution of the homogeneous spin textures in 1D wires initially oriented perpendicular to a QW plane under various in-plane magnetic field angles. The results indicate that both the spin-relaxation rate and precession frequency become anisotropic depending on the SO and in-plane magnetic field orientations. We further extend the anisotropic spin dynamics for arbitrary magnetic field orientation and obtain the exact eigenvalues under a moderately strong SO magnetic field. Based on these theoretical understandings, we prepared 800-nm-width wires along the $[\bar{1}10]$, $[100]$, and $[110]$ crystal orientations based on a GaAs/AlGaAs QW and employ time-resolved Kerr rotation microscopy to evaluate the spin-relaxation time and precession frequency under various in-plane magnetic field angles. For $[110]$ ($[\bar{1}10]$)-oriented wires where both the Rashba and Dresselhaus SO fields are perpendicular to the wire direction but are mutually parallel (antiparallel), the longest spin-relaxation time and the smallest precession frequencies are observed when the in-plane magnetic field is perpendicular to the SO field. An in-plane magnetic field parallel to the SO field has the shortest spin-relaxation time and highest precession frequency. This finding indicates that the maximum spin-relaxation time is exhibited for an in-plane magnetic field parallel to the wire, and the maximum Larmor-precession frequency occurs when this field is perpendicular to the wire. However, because the two SO fields are mutually orthogonal in the $[100]$ wires, the observed anisotropies on the spin relaxation and frequency are tilted at an angle to the wire direction. These experimental results are in excellent agreement with the predictions according to our proposed theory. By fitting the experimentally obtained precession frequency with the value obtained based on the relevant theory, we obtain the Rashba and Dresselhaus SO coefficients. These are in excellent agreement with the values extracted independently from the spatiotemporal dynamics under diffusive spin motion. Therefore, a comprehensive understanding of the spin-relaxation mechanism and interaction between the SO and in-plane magnetic fields can be elucidated by the anisotropic spin dynamics in the wire.

This paper is organized as presented below. In Sec. II, we define the Hamiltonian in a $[001]$ -oriented 2D electron gas with a zinc-blende structure under both Rashba and Dresselhaus SO interactions. Next, in Sec. III, we introduce the spin diffusion equation to consider the homogeneous spin textures in narrow wire structures. In Sec. IV, we describe the time evolution of an initial spin texture which is homogeneous and parallel to the $[001]$ crystal orientation. We examine two distinct cases for which the corresponding in-plane magnetic field is either parallel or perpendicular to the SO field and derive the spin-relaxation rates and precession frequencies explicitly. We further extend the induced anisotropy of the relaxation rate and frequency for arbitrary magnetic field direction. In Sec. V, we introduce the sample structure and evaluate the SO coefficients through the spin dynamics under diffusive spin motion. In Sec. VI, we present the anisotropic spin relaxation and precession dynamics in wire structures along the $[\bar{1}10]$, $[100]$, and $[110]$ crystal orientations for various in-plane magnetic field angles. We close the paper in Sec. VII with the conclusion.

II. HAMILTONIAN

We consider a $[001]$ -oriented 2D electron gas (2DEG) with a zinc-blende structure in the coordinate system Σ where the Cartesian basis vectors $\{\hat{x}, \hat{y}, \hat{z}\}$ are aligned with the crystallographic axes $\hat{x} \parallel [110]$, $\hat{y} \parallel [\bar{1}10]$, $\hat{z} \parallel [001]$. Near the Γ point, the energy dispersion of the 2DEG is described by the following Hamiltonian as

$$\mathcal{H} = \mathcal{H}_{\text{kin}} + \mathcal{H}_z + \mathcal{H}_{\text{SO}}, \quad (1)$$

with the kinetic part $\mathcal{H}_{\text{kin}} = \hbar^2 k^2 / (2m^*)$, where $\mathbf{k} = (k_x, k_y)$ represents the in-plane wave vector and m^* stands for the effective mass. We further include the effects of the *in-plane* magnetic field $\mathbf{B} \perp \hat{z}$, which becomes solely manifest in the Zeeman Hamiltonian as

$$\mathcal{H}_z = \boldsymbol{\omega} \cdot \mathbf{s}, \quad (2)$$

where $\boldsymbol{\omega} = g_{\text{eff}} \mu_B \mathbf{B} / \hbar$ constitutes the Larmor frequency, g_{eff} is the effective g factor, μ_B represents the Bohr magneton, and $\mathbf{s} = \hbar \boldsymbol{\sigma} / 2$ is the spin vector with $\boldsymbol{\sigma} = (\sigma_x, \sigma_y, \sigma_z)$ being the vector of the Pauli matrices. The SO Hamiltonian of

$$\mathcal{H}_{\text{SO}} = \boldsymbol{\Omega}(\mathbf{k}) \cdot \mathbf{s} \quad (3)$$

includes a \mathbf{k} -dependent Zeeman field $\boldsymbol{\Omega} = \boldsymbol{\Omega}_1 + \boldsymbol{\Omega}_3$ called the SO field. The latter is typically decomposed with respect to the wave vector in first and third angular harmonics, respectively, as $\boldsymbol{\Omega}_1$ and $\boldsymbol{\Omega}_3$. Using the in-plane polar coordinates $k_x = k \cos(\varphi)$ and $k_y = k \sin(\varphi)$, where the polar angle φ is measured from the $[110]$ (\hat{x}) axis, the SO field $\boldsymbol{\Omega}_1$ can be written as [31,32]

$$\boldsymbol{\Omega}_1(\varphi) = \frac{2\gamma(\varphi)}{\hbar} k \hat{\boldsymbol{\Omega}}_1(\varphi), \quad (4)$$

with the SO field direction $\hat{\boldsymbol{\Omega}}_1$,

$$\hat{\boldsymbol{\Omega}}_1(\varphi) = \frac{1}{\gamma(\varphi)} \begin{pmatrix} (\alpha + \beta_1) \sin \varphi \\ (-\alpha + \beta_1) \cos \varphi \\ 0 \end{pmatrix}, \quad (5)$$

and the effective SO strength

$$\gamma(\varphi) = [\alpha^2 + \beta_1^2 - 2\alpha\beta_1 \cos(2\varphi)]^{1/2}. \quad (6)$$

The third angular harmonic part of the SO field is

$$\mathbf{\Omega}_3(\varphi) = \frac{2\beta_3}{\hbar} k \begin{pmatrix} \sin(3\varphi) \\ -\cos(3\varphi) \\ 0 \end{pmatrix}. \quad (7)$$

The coefficient $\alpha = \gamma_R \mathcal{E}_z$ denotes the Rashba coefficient and $\beta_1 = \gamma_D (\langle k_z^2 \rangle - \frac{1}{4} k^2)$ and $\beta_3 = \frac{1}{4} \gamma_D k^2$ denotes the Dresselhaus coefficient, respectively. These are attributable to the first and third angular harmonics in the wave vector. The prefactors $\gamma_{R,D}$ are material specific and can be extracted from experiments or calculated using perturbation theory [33]. The term $\langle k_z^2 \rangle$ constitutes the projection of the operator $-\partial_z^2$ on the lowest subband in the growth direction and is inversely proportional to the QW width. The Rashba coefficient α scales with the electric field \mathcal{E}_z because of the potential gradient across the quantum well. Both fields $\mathbf{\Omega}_1$ and $\mathbf{\Omega}_3$ lie in the QW plane. Although the magnitude of $\mathbf{\Omega}_1$ depends on the angle φ , the magnitude of $\mathbf{\Omega}_3$ is isotropic.

III. SPIN-DIFFUSION EQUATION

A. General expression for weak disorder and spin-orbit interaction

In the following, we specifically examine the expected value of the local spin density $\mathbf{s}(\mathbf{r}, t) = \langle \psi^\dagger(\mathbf{r}, t) \mathbf{s} \psi(\mathbf{r}, t) \rangle$ at time t and position \mathbf{r} [or in reciprocal space $\tilde{\mathbf{s}}(\mathbf{q}, t) = \int d\mathbf{r} e^{-i\mathbf{q}\cdot\mathbf{r}} \mathbf{s}(\mathbf{r}, t)$ with wave vector \mathbf{q}], where $\psi(\mathbf{r}, t)$ denotes the fermionic wave function (bispinor) in the ground state. To include the random disorder scattering effects, an average is performed over all spin-independent impurity configurations. Specific examination of the diffusive regime has revealed that the temporal evolution of the spin density follows the spin-diffusion equation, which reads in reciprocal space [31,32,34,35]

$$\frac{d\tilde{\mathbf{s}}(\mathbf{q}, t)}{dt} = \Lambda(\mathbf{q})\tilde{\mathbf{s}}(\mathbf{q}, t). \quad (8)$$

The quantity Λ is called the spin-diffusion operator, and is defined as

$$\Lambda(\mathbf{q}) = -D_s \mathbf{q}^2 + \frac{2\hbar\tau}{im^*} \langle (\mathbf{k} \cdot \mathbf{q}) [\mathbf{\Omega}_1(\mathbf{k})]_\times \rangle + [\boldsymbol{\omega}]_\times - \hat{\tau}_{\text{DP}}^{-1}(\boldsymbol{\Omega}), \quad (9)$$

which involves the d -dimensional diffusion constant $D_s = v_F^2 \tau / d$, later limited to the $d = 2$ case, with Fermi (F) velocity $v_F = \hbar k_F / m^*$, and elastic scattering time τ . At zero temperature, the mean $\langle \cdot \rangle$ constitutes the average over all directions of the wave vector \mathbf{k}_F at the approximately circular Fermi surface. For convenience, we use the matrix representation of the vector product of two vectors \mathbf{a} and \mathbf{b} , i.e., $\mathbf{a} \times \mathbf{b} = [\mathbf{a}]_\times \mathbf{b}$, where $([\mathbf{a}]_\times)_{nm} = \epsilon_{nlm} a_l$ with the antisymmetric Levi-Civita tensor ϵ_{nlm} and a summation over reappearing indices is implied. The first term on the right-hand side of Eq. (9) describes the free diffusion. The second and third terms, respectively, account for spin precession in the space and time domain because of the SO and the magnetic field. It is noteworthy

that only the first angular harmonic SO field $\mathbf{\Omega}_1$ contributes to the spatial spin precession because higher angular harmonics cancel out upon averaging over the Fermi surface. The spin-precession length is defined as the length scale necessary for a spin vector to perform an entire rotation. Because of the φ dependence of $\|\mathbf{\Omega}_1\| \propto \gamma(\varphi)$, the spin-precession length L_n depends on the wave-vector direction $\mathbf{k} = k_F \hat{\mathbf{n}}$ and reads $L_n = 2\pi v_F / \|\mathbf{\Omega}_1(\mathbf{k} = k_F \hat{\mathbf{n}})\|$. The last term on the right-hand side of Eq. (9) represents the DP spin-relaxation tensor [16]

$$[\hat{\tau}_{\text{DP}}^{-1}(\boldsymbol{\Omega})]_{ij} = \tau (\langle \Omega^2 \rangle \delta_{ij} - \langle \Omega_i \Omega_j \rangle), \quad (10)$$

which engenders the exponential decay of a spin texture which is homogeneous in real space ($q = 0$). The spin-diffusion equation (8) is valid for weak disorder and SO coupling, meaning that the Fermi wavelength $\lambda_F = 2\pi / k_F$ is much smaller than the elastic mean free path $l_e = v_F \tau$, whereas the SO-induced spin-precession length L_n is much greater than the mean free path. Furthermore, the expression assumes unbound diffusion in d dimensions. To employ the spin-diffusion equation to a finite-sized geometry such as in a thin film or a narrow wire, we must include boundary effects. These are discussed in the following section.

B. Spin-diffusion operator for homogeneous spin textures in narrow wires

As described herein, we are interested in the spin dynamics of homogeneous spin textures in narrow wires based on a [001]-confined 2DEG. The notion of “narrow” here means that the wire width W is much less than the spin-precession length L_u in the direction $\hat{\mathbf{u}}$ of the lateral boundaries at $r_u = \pm W/2$. This condition is regarded as spin reflecting. At the same time, the wire width is presumed to be sufficiently wide, such that (i) it exceeds the elastic mean free path l_e , allowing the transverse motion to remain diffusive, and (ii) the quantum size effects attributable to the boundary on the energy dispersion are irrelevant. Condition (ii), which becomes significant if $\lambda_F \sim W$, is already implied by (i) because of our earlier assumption that $\lambda_F \ll l_e < W$. Let us define the wire direction as determined by the unit vector $\hat{\mathbf{g}} := (\cos(\phi), \sin(\phi), 0) = \hat{\mathbf{z}} \times \hat{\mathbf{u}}$ with the in-plane polar angle ϕ , as measured from [110]. As explained at length in the Appendix, for the limit $W/L_u \rightarrow 0$, aside from $\mathbf{\Omega}_3$, only the part of the SO field $\mathbf{\Omega}_1$ with wave-vector components along the wire direction $\hat{\mathbf{g}}$ contributes to spin relaxation. In this case, the spin-diffusion operator (9) reduces to the following:

$$\Lambda_0(q) = [\boldsymbol{\omega}]_\times - D_s \left\{ q \hat{\mathbf{g}} + \frac{2\pi i}{L_g} [\hat{\boldsymbol{\Omega}}_1(\phi)]_\times \right\}^2 - \hat{\tau}_{\text{DP}}^{-1}(\boldsymbol{\Omega}_3). \quad (11)$$

To analyze the spin-density dynamics, a new coordinate frame Σ' is selected. This is adapted to the orientation of $\mathbf{\Omega}_1$, which has the following underlying basis vectors: $\{\hat{\boldsymbol{\Omega}}_1(\phi), \hat{\mathbf{z}} \times \hat{\boldsymbol{\Omega}}_1(\phi), \hat{\mathbf{z}}\}$. In system Σ' , the spin-diffusion operator for a homogeneous ($q = 0$) spin texture becomes

$$\Lambda_0 = \begin{pmatrix} -\Delta_3 & 0 & \omega_\perp \\ 0 & -\Delta_1(\phi) - \Delta_3 & -\omega_\parallel \\ -\omega_\perp & \omega_\parallel & -\Delta_1(\phi) - 2\Delta_3 \end{pmatrix}, \quad (12)$$

with the spin-relaxation rates

$$\Delta_1(\phi) = 2\tau \left(\frac{\gamma(\phi)k_F}{\hbar} \right)^2, \quad (13)$$

$$\Delta_3 = 2\tau \left(\frac{\beta_3 k_F}{\hbar} \right)^2. \quad (14)$$

Here, we defined $\omega_{\parallel} = \omega \cos \theta$ and $\omega_{\perp} = \omega \sin \theta$ with $\theta = \angle(\boldsymbol{\omega}, \boldsymbol{\Omega}_1)$ as components of the Larmor frequency $\boldsymbol{\omega}$, which are parallel and perpendicular, respectively, to the SO field $\boldsymbol{\Omega}_1(\phi)$. To relate resulting expressions to the original crystal-adherent coordinate frame Σ , where the Larmor frequency vector is given as $\boldsymbol{\omega} = \omega(\cos \vartheta, \sin \vartheta, 0)$ with the polar angle ϑ measured from the $\hat{\mathbf{x}} \parallel [110]$ axis, we use the relation

$$\theta = \vartheta - \chi, \quad (15)$$

where $\chi = \arctan(\Omega_y/\Omega_x)$ is the polar angle enclosed by $\boldsymbol{\Omega}_1$ and the $[110]$ crystal direction ($\hat{\mathbf{x}}$). An arbitrary vector \mathbf{v}' in Σ' can be represented in Σ by applying the transformation $\mathbf{v} = \mathcal{R}\mathbf{v}'$ with the rotation matrix

$$\mathcal{R} = \begin{pmatrix} \cos \chi & -\sin \chi & 0 \\ \sin \chi & \cos \chi & 0 \\ 0 & 0 & 1 \end{pmatrix}. \quad (16)$$

To convert scalar expressions, such as eigenvalues, the identity

$$\cos \theta = \hat{\boldsymbol{\Omega}}_1 \cdot \hat{\boldsymbol{\omega}} = \frac{\alpha \sin(\vartheta - \phi) - \beta_1 \sin(\vartheta + \phi)}{\gamma(\phi)} \quad (17)$$

is particularly convenient. The spin-diffusion operator (12) constitutes a dynamic matrix that solves the linear differential equation $\partial_t \tilde{\mathbf{s}} = \Lambda_0 \tilde{\mathbf{s}}$, where a general solution can be written as $\tilde{\mathbf{s}}(t) = \exp(\Lambda_0 t) \tilde{\mathbf{s}}(0)$. The dynamic matrix Λ_0 separates into a Hermitian part (in the chosen basis even diagonal) and a skew-symmetric part. The Hermitian part is comprised of spin-relaxation rates and yields negative semidefinite eigenvalues, and therefore describes a decaying of the constant spin texture. The skew-symmetric part includes the Larmor-precession frequencies and yields imaginary eigenvalues, thereby causing time-periodic orbits. The mixing of both parts in Λ_0 engenders generally complex eigenvalues λ_n ($n \in \{0, \pm\}$), where the real part defines an effective spin-relaxation rate

$$\frac{1}{\tau_{s,n}} := |\operatorname{Re} \lambda_n|, \quad (18)$$

and the imaginary part defines an effective Larmor frequency

$$v_n := |\operatorname{Im} \lambda_n|. \quad (19)$$

Both $1/\tau_{s,n}$ and v_n can be influenced, respectively, by the Larmor frequency ω and the spin-relaxation rates $\Delta_{1,3}$. Importantly, the relative significance is found by the ratio $\omega/\Delta_{1,3}$ between the Larmor frequency and spin-relaxation rates, and *not* by the relative strength of the magnetic and SO fields.

We do not account for spin relaxation at the boundaries because the DP mechanism is dominant in zinc-blende semiconductor wires. Spin relaxation due to the Elliot-Yafet (EY) mechanism at the boundaries is not sensitive to changes in the in-plane magnetic field orientation. Rather, it is expected

that the EY mechanism gives an additive spin-relaxation rate over all in-plane field angles. In previous studies, the effect of the EY mechanism in the wire has been discussed [36,37]. The spin-flip process at the boundary suppressed the highly polarized spin polarization near the wire edge [36]. Also, more frequent boundary collision in the narrow wire enhances spin relaxation [37].

In the QW structures, the cubic Dresselhaus coefficient is usually smaller than the linear Dresselhaus coefficient. As we will show later, the physical picture in the experiments does not require the Δ_3 term and only considers the Δ_1 term in the analysis. However, it should be noted that since the relative contribution of the Δ_3 term depends on the α/β_1 ratio, wire direction, and the investigated initial spin state, it is erroneous to believe that the Δ_3 term is irrelevant.

IV. DYNAMICS OF A HOMOGENEOUS (001)-ORIENTED SPIN TEXTURE

In the following, we analyze the time evolution of an initial spin texture that is at time $t = 0$ homogeneous in real space and which is parallel to the $[001]$ crystal orientation, i.e., $\mathbf{s}(0) = \hat{\mathbf{z}}$. We first present exact solutions for the special cases in which the magnetic field is either parallel or perpendicular to the SO field direction $\hat{\boldsymbol{\Omega}}_1(\phi)$. Thereafter, we concentrate on the low-damping regime, where the Larmor precession of the spin texture is observable. In this regime, we can derive simple analytic formulas for the effective spin-relaxation rates and oscillation frequencies that are valid for arbitrary directions of the in-plane magnetic field. For enhanced precision, we also provide a more generally applicable analytic expression which provides accurate values for high and moderately high magnetic fields.

A. Magnetic field parallel to the SO field

For cases in which the magnetic field is parallel to the SO field, i.e., $\omega_{\perp} = 0$, the eigenvalues of Λ_0 read as

$$\lambda_0 = -\Delta_3, \quad (20)$$

$$\lambda_{\pm} = -\Delta_1 - \frac{3}{2}\Delta_3 \pm i\xi_{\parallel}, \quad (21)$$

with the corresponding (non-normalized) eigenvectors

$$\mathbf{v}_0 = (1, 0, 0), \quad (22)$$

$$\mathbf{v}_{\pm} = (0, \Delta_3 \pm 2i\xi_{\parallel}, 2\omega_{\parallel}), \quad (23)$$

where $\xi_{\parallel} = \sqrt{\omega_{\parallel}^2 - \Delta_3^2/4}$. We identify two parameter regimes: (i) $\Delta_3 < 2\omega_{\parallel}$, which implies that $\operatorname{Im} \xi_{\parallel} = 0$; and (ii) $\Delta_3 > 2\omega_{\parallel}$, which implies that $\operatorname{Re} \xi_{\parallel} = 0$. In case (i), the term ξ_{\parallel} constitutes an effective Larmor frequency, which depends on the spin-relaxation rate Δ_3 . In case (ii), the term $i\xi_{\parallel}$ contributes to the total effective spin-relaxation rate that is, as a result, frequency dependent. It is noteworthy that the eigenvectors are nonorthogonal because Λ_0 is not Hermitian. The time evolution of an initial spin orientation out of plane is

given as

$$\begin{aligned} \mathbf{s}(t) &= \frac{1}{4\omega_{\parallel}} \sum_{\pm} \left(1 \pm i \frac{\Delta_3}{2\xi_{\parallel}} \right) \mathbf{v}_{\pm} e^{\lambda_{\pm} t} \\ &= \exp \left[- \left(\Delta_1 + \frac{3}{2} \Delta_3 \right) t \right] \sin(\xi_{\parallel} t) \\ &\quad \times \left(0, -\frac{\omega_{\parallel}}{\xi_{\parallel}}, \cot(\xi_{\parallel} t) - \frac{\Delta_3}{2\xi_{\parallel}} \right). \end{aligned} \quad (24)$$

For measurements of the z component of the spin density at time t , we expect

$$s_z(t) = e^{\text{Re}\lambda_{\pm} t} \left[\cos(\text{Im}\lambda_{\pm} t) + \frac{\text{Re}\lambda_0}{2\text{Im}\lambda_{\pm}} \sin(\text{Im}\lambda_{\pm} t) \right]. \quad (25)$$

B. Magnetic field perpendicular to the SO field

For the case in which the magnetic field is perpendicular to the SO field, i.e., $\omega_{\parallel} = 0$, the eigenvalues of Λ_0 read as

$$\lambda_0 = -\Delta_1 - \Delta_3, \quad (26)$$

$$\lambda_{\pm} = -\frac{1}{2}(\Delta_1 + 3\Delta_3) \pm i\xi_{\pm}, \quad (27)$$

where $\xi_{\pm} = \sqrt{\omega_{\perp}^2 - (\Delta_1 + \Delta_3)^2/4}$ with the corresponding (non-normalized) eigenvectors

$$\mathbf{v}_0 = (0, 1, 0), \quad (28)$$

$$\mathbf{v}_{\pm} = (\lambda_{\mp} + \Delta_3, 0, \omega_{\perp}). \quad (29)$$

Similar to the discussion above, ξ_{\pm} denotes an effective Larmor frequency assuming that $\Delta_1 + \Delta_3 < 2\omega_{\perp}$, and otherwise ξ_{\pm} contributes to the spin relaxation. The time evolution of an initial spin orientation out of plane is given as

$$\begin{aligned} \mathbf{s}(t) &= \frac{1}{2i\xi_{\pm}\omega_{\perp}} \sum_{\pm} \pm(\Delta_3 + \lambda_{\pm}) \mathbf{v}_{\pm} e^{\lambda_{\pm} t} \\ &= \exp \left[-\frac{1}{2}(\Delta_1 + 3\Delta_3)t \right] \sin(\xi_{\pm} t) \\ &\quad \times \left(\frac{\omega_{\perp}}{\xi_{\pm}}, 0, \cot(\xi_{\pm} t) - \frac{\Delta_1 + \Delta_3}{2\xi_{\pm}} \right). \end{aligned} \quad (30)$$

For measurement of the z component of the spin density at time t , the result is equivalent to Eq. (25) when eigenvalues (20) and (21) are replaced, respectively, by Eqs. (26) and (27).

C. Low-damping regime for arbitrary magnetic field orientation

The spin-relaxation rates were demonstrated earlier to become frequency independent after exceeding the threshold $2\omega_{\perp} \geq \Delta_1 + \Delta_3$ for a magnetic field perpendicular and $2\omega_{\parallel} \geq \Delta_3$ for a magnetic field parallel to the SO field $\Omega_1(\phi)$. Asymptotically, we can thereby find simple analytic frequency-independent expressions for the spin-relaxation rates for *arbitrary* magnetic field directions which are generally valid in the low-damping regime. In the limit $\omega \gg \Delta_1 + \Delta_3$, the eigenvectors of the spin-diffusion operator (12) are determined predominantly by magnetic-field-dependent terms. Neglecting Δ_1 and Δ_3 , the eigenvalues

are

$$\lambda_0^{(0)} = 0, \quad (31)$$

$$\lambda_{\pm}^{(0)} = \pm i\omega, \quad (32)$$

with the respective eigenvectors

$$\mathbf{v}_0^{(0)} = (\cos\theta, \sin\theta, 0), \quad (33)$$

$$\mathbf{v}_{\pm}^{(0)} = \pm(-i\sin\theta, i\cos\theta, \pm 1)/\sqrt{2}. \quad (34)$$

It is noteworthy that the eigenvalue $\lambda_0^{(0)}$ vanishes because the related eigenvector corresponds to a spin orientation parallel to the magnetic field, which does not oscillate in time. By treating the spin-relaxation contributions Δ_1 and Δ_3 as a weak perturbation, we can compute the approximate eigenvalues within standard perturbation theory. Including corrections up to the second order, we estimate that

$$\lambda_n \approx \sum_{j=0}^2 \lambda_n^{(j)} \quad \text{with } n \in \{0, \pm\}. \quad (35)$$

We find that the first-order corrections

$$\lambda_0^{(1)} = -\Delta_1 \sin^2\theta - \Delta_3, \quad (36)$$

$$\lambda_{\pm}^{(1)} = -\frac{\Delta_1}{2}[1 + \cos^2(\theta)] - \frac{3}{2}\Delta_3 \quad (37)$$

display spin-relaxation anisotropy because of the presence of an in-plane magnetic field, whereas the (nonvanishing) second-order corrections

$$\lambda_{\pm}^{(2)} = \pm \frac{i}{8\omega} [3\Delta_1^2 \sin^4\theta - 2\Delta_1(2\Delta_1 + \Delta_3) \sin^2\theta - \Delta_3^2], \quad (38)$$

together with the zeroth-order terms $\lambda_{\pm}^{(0)}$ reproduce the spin-relaxation-dependent effective Larmor frequency. In short, the effective spin-relaxation rates and Larmor frequencies in the low-damping regime are given as

$$\tau_{s,0\pm}^{-1} \approx |\text{Re}\lambda_{0,\pm}^{(1)}| \quad (39)$$

and

$$v_{\pm} \approx |\text{Im}(\lambda_{\pm}^{(0)} + \lambda_{\pm}^{(2)})|, \quad (40)$$

respectively. As shown in Fig. 1, we compare these results with the exact eigenvalues obtained by the diagonalization of Λ_0 in Eq. (12). Although the low-damping limit has an associated assumption of $\omega \gg \Delta_1 + \Delta_3$, remarkable agreement is obtained even for $\omega \approx \Delta_1 + \Delta_3$. Next we use earlier results to compute approximate formulas for the time evolution of the initial spin texture $\mathbf{s}(0) = (0, 0, 1)$ for arbitrary magnetic field directions. The initial spin texture can be represented by the approximate eigenvectors as

$$\mathbf{s}(0) = \frac{1}{2}[\mathbf{v}_+^{(0)} + \mathbf{v}_-^{(0)}], \quad (41)$$

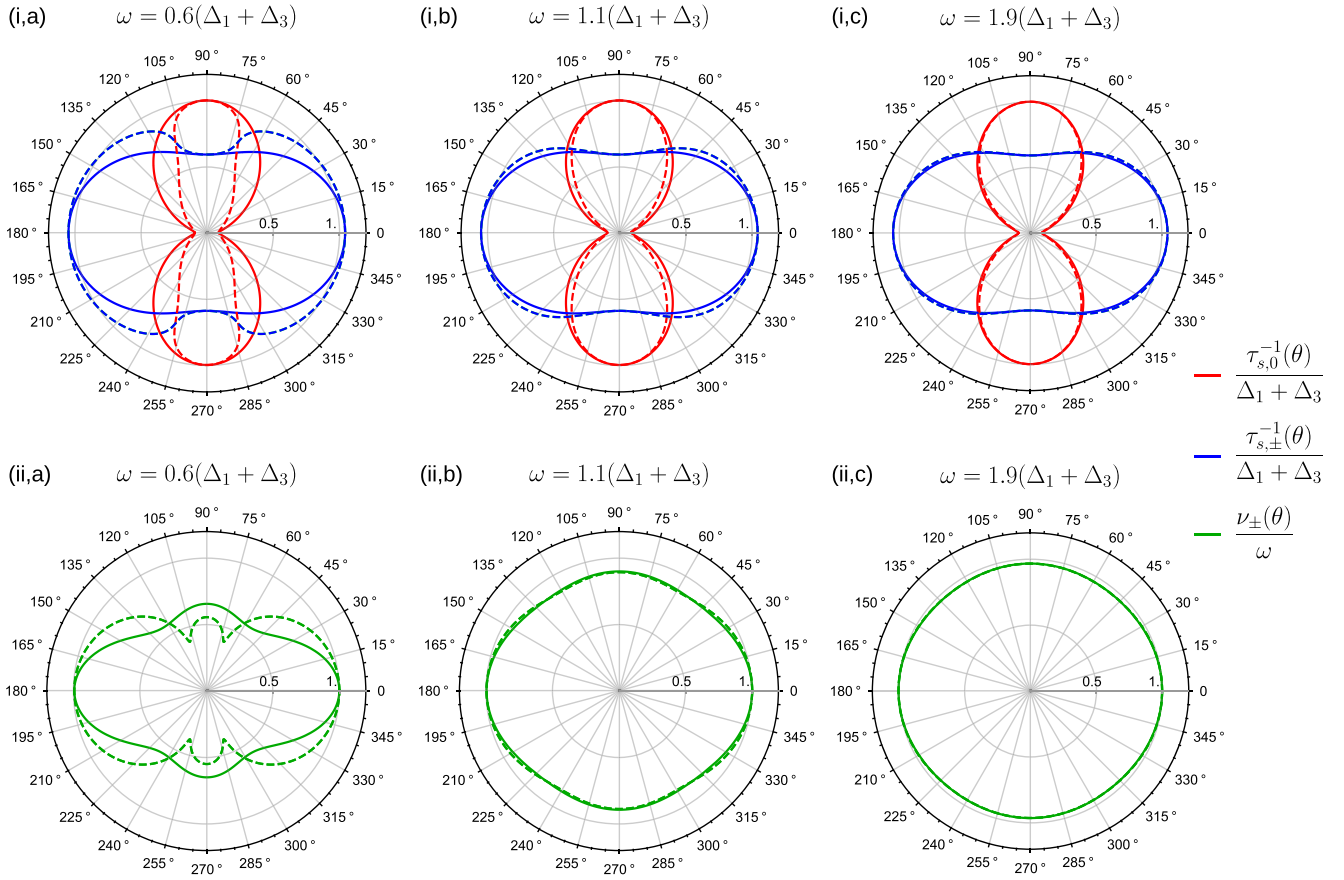


FIG. 1. Effective spin-relaxation rates $1/\tau_{s,0,\pm} = |\text{Re}\lambda_{0,\pm}|$ [row (i)] and Larmor frequencies $\nu_{\pm} = |\text{Im}\lambda_{\pm}|$ ($\nu_0 = 0$) [row (ii)] in dependence of the in-plane magnetic field angle θ for different magnitudes of the Larmor frequency ω [columns (a),(b),(c)] and for the ratio of the first and third angular harmonic spin-relaxation terms $\Delta_3/\Delta_1 = 0.1$. The solid lines show the approximate spin-relaxation rates in the low-damping regime using Eq. (35) and the dashed lines display the real and imaginary parts of the exact eigenvalues given in Eqs. (48) and (52) obtained by diagonalizing the matrix (12).

which yields finite time t for a large magnetic field

$$\begin{aligned} \mathbf{s}(t) &\approx \frac{1}{2}[e^{\lambda_+ t} \mathbf{v}_+^{(0)} + e^{\lambda_- t} \mathbf{v}_-^{(0)}] \\ &\approx \exp\left(-\frac{t}{\tau_{s,\pm}}\right)(\sin \theta \sin \nu_{\pm} t, -\cos \theta \sin \nu_{\pm} t, \cos \nu_{\pm} t). \end{aligned} \quad (42)$$

Consequently, the dynamics are determined by the eigenvalues λ_{\pm} . Because the magnitudes of the real and imaginary parts of λ_{\pm} are degenerate, the decay and oscillations can be described using a single relaxation rate and frequency. The spin-relaxation anisotropy engenders a change of the effective spin lifetime

$$\delta\tau_{s,\pm} = \frac{2\Delta_1 \sin^2 \theta}{(2\Delta_1 + 3\Delta_3)(\Delta_1 + \Delta_1 \cos^2 \theta + 3\Delta_3)}, \quad (43)$$

where $\delta\tau_{s,\pm} = \tau_{s,\pm} - \tau_{s,\pm}^{\min}$ with $\tau_s^{\min} = \tau_s(\theta = 0)$. It is also interesting that, for $\Delta_1 > \Delta_3$, the frequency ν_{\pm} assumes a global minimum

$$\nu_{\pm, \min} = \omega - \frac{1}{6\omega}(\Delta_1^2 + \Delta_1 \Delta_3 + \Delta_3^2) \quad (44)$$

appearing at the angles

$$\theta_{\min} = \pm \arctan \sqrt{\frac{2\Delta_1 + \Delta_3}{\Delta_1 - \Delta_3}} \pmod{\pi}, \quad (45)$$

which is illustrated by the example presented in Fig. 2. This appearance leads to a change of the effective Larmor frequency, such that

$$\delta\nu_{s,\pm} = \nu_{s,\pm} - \nu_{\pm, \min} = \frac{(\Delta_3 - \Delta_1 + 3\Delta_1 \cos^2 \theta)^2}{24\omega}. \quad (46)$$

The difference between the global minimum and the adjacent local maximum is given as

$$\nu_{\pm}(\pi/2) - \nu_{\pm, \min} = \frac{(\Delta_1 - \Delta_3)^2}{24\omega}, \quad (47)$$

and therefore disappears for $\Delta_3 \rightarrow \Delta_1$. In Fig. 3, modulation of the effective spin lifetime $\delta\tau_{s,\pm}$ and Larmor frequency $\delta\nu_{\pm}$ are shown in terms of the dependence of the polar angle ϑ [see Eq. (15)] of the in-plane magnetic field and the distinct wire directions in the crystal-adherent coordinate system Σ .

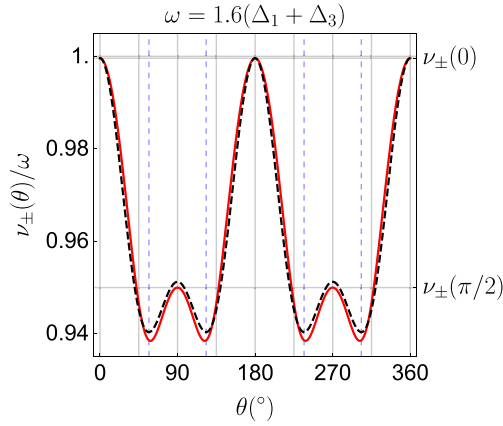


FIG. 2. The effective Larmor frequency $\nu_{\pm}(\theta) = |\text{Im}\lambda_{\pm}|$ and the dependence of the in-plane magnetic field angle θ for $\omega = 1.6(\Delta_1 + \Delta_3)$. The red solid line corresponds to Eq. (52), i.e., the imaginary part of the respective eigenvalue obtained by the exact diagonalization of expression (12). The black dashed line represents the approximation in the low-damping regime, Eq. (35). The blue dashed grid lines correspond to the approximate angle θ_{\min} [Eq. (45)], for which a global minimum is assumed.

D. Exact eigenvalues for moderately strong magnetic fields

Because of large SO coupling in certain materials, it may be challenging to achieve the low-damping regime. Expressions for spin relaxation that are more precise and frequency anisotropy with a range that covers a larger parameter spectrum can be useful to support the fitting of data obtained from experimentation. As a result of the mixing of SO coupling and the magnetic field, the exact eigenvalues are generally complex. Moreover, the disentangling of real and imaginary parts is intricate. By inspection, we find exact expressions for the effective spin-relaxation rates and Larmor frequencies that hold for $\xi := \Delta_1/\omega \leq \sqrt{3}/\sqrt{1 + \epsilon + \epsilon^2}$, where $\epsilon = \Delta_3/\Delta_1$. Assuming that $\Delta_1 > \Delta_3$, this condition simplifies to $\omega > \Delta_1/\sqrt{3} \approx 0.58\Delta_1$. Therefore, the following formulas also cover moderately large frequencies and extend the results presented in an earlier section. In this regime, the exact diagonalization of Eq. (12) yields the effective spin-relaxation rates

$$\frac{\tau_{s,n}^{-1}}{\omega} = \frac{2}{3}\xi(1 + 2\epsilon) + \frac{f(\theta)^{2/3} - \kappa}{6f(\theta)^{1/3}} \begin{cases} -1, & \text{for } n = 0 \\ \frac{1}{2}, & \text{for } n = \pm, \end{cases} \quad (48)$$

where

$$\kappa = 12 - 4(1 + \epsilon + \epsilon^2)\xi^2, \quad (49)$$

$$f(\theta) = g(\theta) + \sqrt{\kappa^3 + g(\theta)^2}, \quad (50)$$

$$g(\theta) = 4\xi\{(2 + \epsilon)[9 + \xi^2(1 + \epsilon - 2\epsilon^2)] - 27\sin^2(\theta)\} \quad (51)$$

and the effective Larmor frequencies

$$\frac{\nu_{\pm}(\theta)}{\omega} = \frac{f(\theta)^{2/3} + \kappa}{4\sqrt{3}f(\theta)^{1/3}}, \quad (52)$$

and $\nu_0 = 0$.

V. SAMPLE STRUCTURE AND SPIN-ORBIT COEFFICIENTS IN GAS/ALGAS TWO-DIMENSIONAL ELECTRON GAS

To clarify the anisotropic spin dynamics under an in-plane magnetic field in narrow wires, we used a 20-nm-thick GaAs/AlGaAs QW grown on a (001) GaAs substrate. The Si-doped $\text{Al}_{0.3}\text{Ga}_{0.7}\text{As}$ layer was placed 35 nm above the GaAs QW layer to make the QW asymmetric, which meant the Rashba SO field was larger than the Dresselhaus field. We fabricated 50 parallel wires along the $[\bar{1}10]$, $[100]$, and $[110]$ crystal orientations by electron beam lithography and reactive ion etching. All wire widths and lengths are, respectively, 800 nm and 150 μm with 1 μm separation between the wires. The wire width is designed to be much shorter than the spin-precession length. The carrier density and mobility were, respectively, $1.72 \times 10^{11} \text{ cm}^{-2}$ and $1.12 \times 10^5 \text{ cm}^2/\text{Vs}$, as evaluated from a separately processed Hall bar device at 4.2 K. For time-resolved Kerr rotation (TRKR) microscopy, we used a mode-locked Ti:sapphire laser which emitted 2-ps-long pulses at a 79.2-MHz repetition rate. The laser was split into pump and probe beams with delay time t . A circularly polarized pump beam with a Gaussian width of σ_{pp} was focused on the sample surface to excite out-of-plane spin polarization, while the linearly polarized probe beam with a spot size of σ_{pr} was overlapped with the pump beam. It detected the z component of excited spin polarization at the delay time t . For TRKR measurements in narrow wires, we set the σ_{pp} and σ_{pr} to be 15 and 30 μm , respectively. Because the spot sizes of the pump and probe beams were larger than both the 800-nm wire width and the spin-precession length, helical spin textures were not excited in this condition. In addition, the nonequilibrium spin population was excited in several wires simultaneously and was detected as spatially averaged spin dynamics. This corresponds to the detection of the homogeneous spin texture discussed in Sec. III B. We applied the constant in-plane magnetic field of $B_{\text{in}} = \|B_{\text{in}}\| = 0.65 \text{ T}$ and rotated its direction as polar angle with respect to the $[110]$ crystal orientation [Fig. 4(a)]. At each B_{in} direction, we applied TRKR microscopy. Before measuring the anisotropic spin dynamics in the wire, we evaluated the Rashba and Dresselhaus SO coefficients for a nonprocessed sample by employing spatiotemporal Kerr rotation microscopy. By changing the relative distance r between the pump and probe beam location using a motor-controlled scanning mirror, we measured the TRKR signal and evaluated the frequency modulation of the spin precession which originated from the diffusion-induced SO field. All the optical measurements were taken at 30 K to suppress dynamic nuclear spin polarization [38].

Considering the theoretical description of spin dynamics developed in Secs. III and IV, the spin-precession length

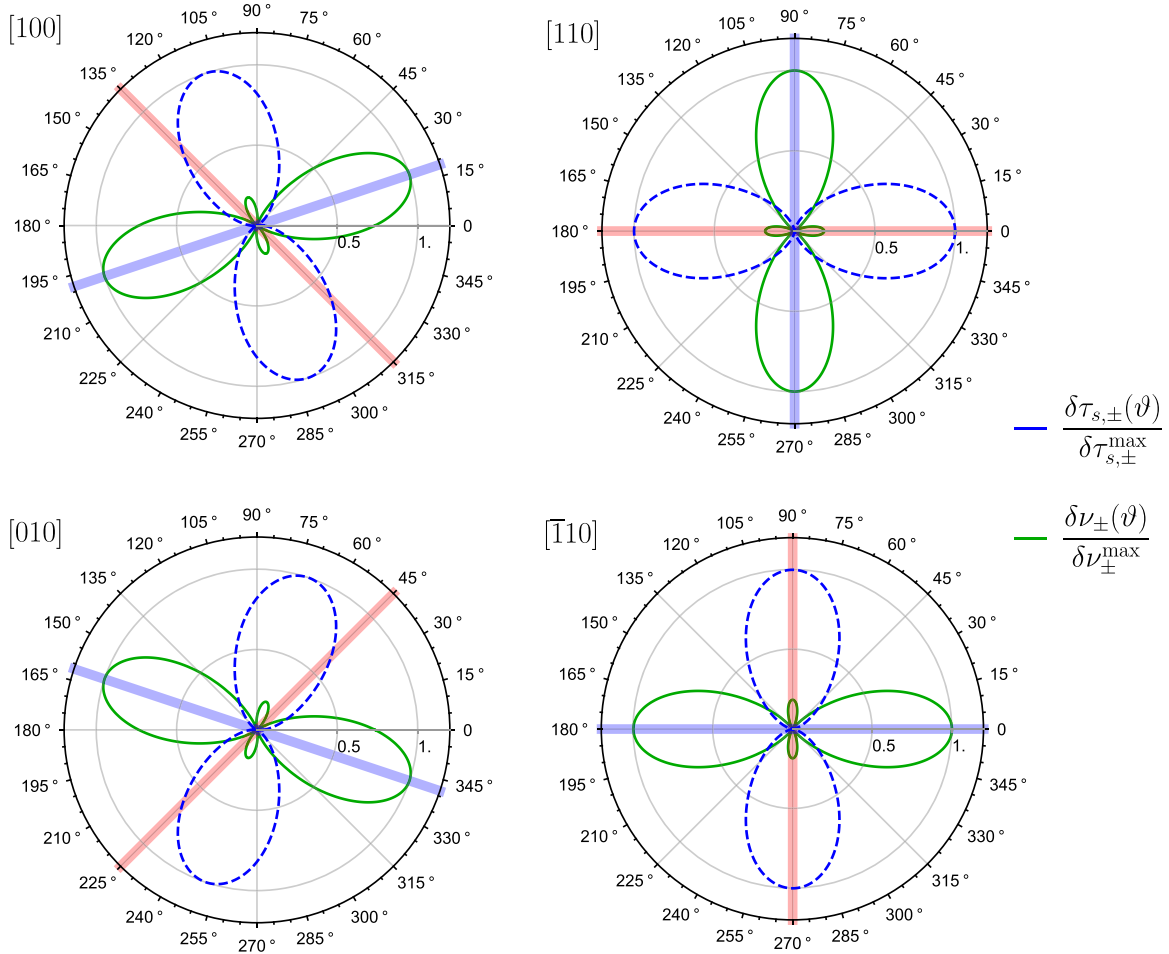


FIG. 3. Modulation of the effective spin lifetime $\delta\tau_{s,\pm}$ [Eq. (43)] (blue dashed lines) and Larmor frequency $\delta\nu_{\pm}$ [Eq. (43)] (green solid line) depending on the in-plane magnetic field angle ϑ (measured from $[110]$) and the wire orientation (indicated by wide red lines and the crystal orientations shown by the plot labels). We select the Larmor frequency and spin-relaxation configuration $\omega = 1.3(\Delta_1 + \Delta_3)$ and $\Delta_3 = 0.1\Delta_1$. We assume a ratio $\alpha/\beta_1 = 2$ between the Rashba and Dresselhaus SO strength which, together with the wire direction, leads to the specific orientation of the SO field Ω_1 (displayed by the wide blue lines).

L_u was expected to be larger than wire width W . To clarify this point, we first investigated the SO coefficients in the present GaAs QW by spatiotemporal Kerr rotation microscopy [Fig. 4(a)]. The spins excited by the pump beam were diffused away from the center position $(0,0)$. At position (x, y) of the probe beam, the diffusion velocity was found as the center-to-center distance r between the pump and probe spots, as described by [39]

$$v_{\text{dif}} = \frac{2D_s}{2D_s\tau_s + \sigma_{\text{eff}}^2} r, \quad (53)$$

where D_s is the spin-diffusion constant, τ_s represents the DP spin-relaxation time, and σ_{eff} denotes the convoluted spot size defined by $\sigma_{\text{eff}}^2 = \sigma_{\text{pp}}^2 + \sigma_{\text{pr}}^2$. The spin-precessional motion is induced by the diffusion velocity v_{dif} under an external magnetic field $\mathbf{B}_{\text{in}} = (B_x, B_y)$, whose precession frequency $\Omega_{x,y}(v_{y,x})$ is described by

$$\Omega_{x,y}(v_{y,x}) = \frac{2m^*}{\hbar^2} (\pm\alpha + \beta_1)v_{y,x} + \frac{g_{\text{eff}}\mu_B}{\hbar} B_{x,y}. \quad (54)$$

By scanning the probe position along $x \parallel [110]$ and $y \parallel [\bar{1}10]$, one can detect the SO-induced frequency modula-

tion $d\Omega_{x,y}(v_{y,x})/dr$, which is proportional to the Rashba and Dresselhaus SO coefficients [Fig. 4(a)]. Figure 4(b) shows the representative color-coded time-space map of TRKR traces along the y scan with $\sigma_{\text{eff}} = 11 \mu\text{m}$ in $\mathbf{B}_{\text{in}} = B_x \hat{x}$ with $B_x = -0.65$ T. The spin-precession frequency is modulated depending on the probe position, and can be attributed to the diffusion-induced SO field. We continued mapping TRKR traces by scanning along both the x and y axes under fixed $B_{\text{in}} = 0.65$ T for different σ_{eff} sizes. Then we extracted the precession frequency $|\Omega_{\text{meas}}|$ by fitting the normalized Kerr signal

$$s_z = \exp\left(-\frac{t}{\tau_s}\right) \cos(|\Omega_{\text{meas}}|t + \zeta), \quad (55)$$

where $|\Omega_{\text{meas}}|$ is the Larmor frequency and ζ is the phase shift. Figure 4(c) shows the evaluated frequency modulation defined by $\Omega_{\text{so}} = |\Omega_{\text{meas}}| - g_{\text{eff}}\mu_B B_{x,y}/\hbar$ as a function of x or y in various σ_{eff} , where the effective g factor is evaluated for both the pump and probe beams at the position $(x, y) = (0, 0)$. The linear variation in Ω_{so} can be attributed to the position-dependent diffusion velocity described by Eq. (54). The corresponding linear slope of Ω_{so} ($d\Omega_{\text{so}}/dr$) reflects the

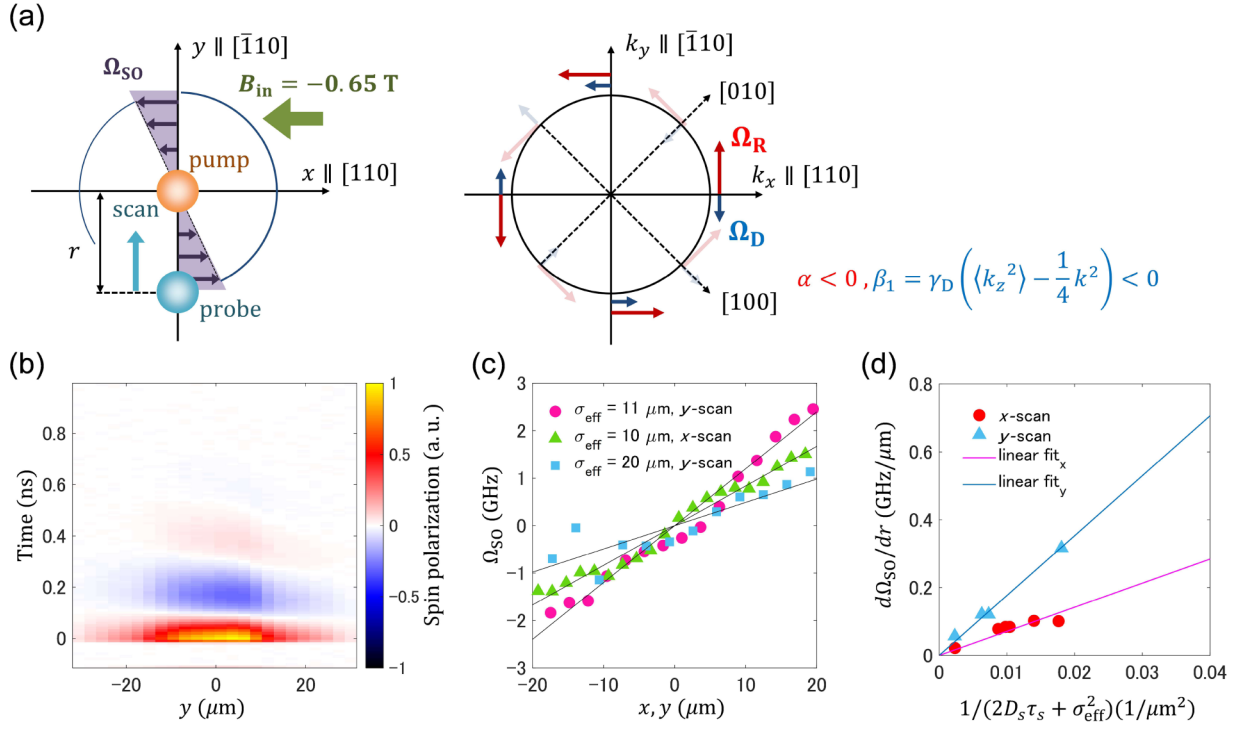


FIG. 4. Methods to evaluate Rashba and Dresselhaus SO coefficients: First, (a) shows that the excited spins by the pump beam are diffused away from the center position (0,0). The diffusion velocity v_{dif} is determined by Eq. (53). The right figure expresses the SO field depending on electron momentum when α and β_1 is negative. Also, (b) shows the color-coded time-space map of TRKR traces along the y scan with $\sigma_{\text{eff}} = 11 \mu\text{m}$ in $B_x = -0.65 \text{ T}$. In (c), the evaluated frequency modulation is depicted as a function of x or y in various σ_{eff} . Panel (d) shows plots $d\Omega_{\text{so}}/dx$ and $d\Omega_{\text{so}}/dy$ as functions of $1/(2D_s\tau_s + \sigma_{\text{eff}}^2)$ to clarify the SO contribution by fitting with Eqs. (56) and (57).

total SO coefficient and the spot size described in Eqs. (53) and (54). This is readily apparent by changing the spot size from $\sigma_{\text{eff}} = 11 \mu\text{m}$ to $20 \mu\text{m}$ for the y -scan measurements in $B_x = -0.65 \text{ T}$ shown as the filled circles and squares, respectively, in Fig. 4(c), where the larger spots induce smaller $d\Omega_{\text{so}}/dr$. In the case of the spots of similar sizes shown as filled circles ($11 \mu\text{m}$, y scan in $B_x = -0.65 \text{ T}$) and triangles ($10 \mu\text{m}$, x scan in $B_y = +0.65 \text{ T}$) in Fig. 4(c), $d\Omega_{\text{so}}/dr$ are reduced in the x -scan measurements because of the subtractive contribution between the Rashba and Dresselhaus SO fields. To quantitatively evaluate the SO contributions, we plot $d\Omega_{\text{so}}/dx$ and $d\Omega_{\text{so}}/dy$ as functions of $1/(2D_s\tau_s + \sigma_{\text{eff}}^2)$ in Fig. 4(d). The value of $D_s = 0.0114 \text{ m}^2/\text{s}$ was ascertained from the spatially resolved expansion of the spin polarization [40]. The linear variation of $d\Omega_{\text{so}}/dr$ in Fig. 4(d) can be described as

$$d\Omega_{\text{so}}/dx = \frac{4m^*D_s}{\hbar^2} \frac{-\alpha + \beta_1}{2D_s\tau_s + \sigma_{\text{eff}}^2}, \quad (56)$$

$$d\Omega_{\text{so}}/dy = -\frac{4m^*D_s}{\hbar^2} \frac{\alpha + \beta_1}{2D_s\tau_s + \sigma_{\text{eff}}^2}. \quad (57)$$

By fitting with Eqs. (56) and (57), we evaluated the Rashba and Dresselhaus SO coefficients as $\alpha = -3.22 \times 10^{-13} \text{ eV m}$ and $\beta_1 = -1.37 \times 10^{-13} \text{ eV m}$, respectively. The minus sign in Eq. (57) reflects the negative value of B_x . The corresponding spin-precession lengths $L_u(\phi)$ are calculated as 8.69, 11.40, and $21.57 \mu\text{m}$, respectively, for the $[\bar{1}10]$, $[100]$, and $[110]$ crystal orientations, all of which are much longer than

the 800-nm-wire width. These findings ensure the condition of 1D diffusive approximation for spin. In addition, the Fermi wavelength and mean free path are evaluated as $\lambda_F = 60 \text{ nm}$ and $l_e = 0.76 \mu\text{m}$, respectively, satisfying the narrow wire condition of $\lambda_F \ll l_e \leq W$.

VI. SPIN DYNAMICS IN WIRE STRUCTURES ALONG THE $[\bar{1}10]$, $[100]$, AND $[110]$ CRYSTAL ORIENTATIONS FOR VARIOUS IN-PLANE MAGNETIC FIELD ANGLES

Next, we investigate the spin dynamics in GaAs/AlGaAs-based wires along the $[\bar{1}10]$, $[100]$, and $[110]$ crystal orientations under the in-plane magnetic field $B_{\text{in}} = 0.65 \text{ T}$ for various $B_{\text{in}}(\vartheta)$ direction, where ϑ is defined from the $x \parallel [110]$ orientation [Fig. 5(a)].

Figure 5(b) shows the color-coded plot of TRKR amplitude as functions of the $B_{\text{in}}(\vartheta)$ direction and delay time t in the $[110]$ wire. The directions of $B_{\text{in}}(\vartheta = 90^\circ)$ and $B_{\text{in}}(\vartheta = 180^\circ)$ correspond to $(B_{\text{in}} \perp [110])$, which is perpendicular, and $(B_{\text{in}} \parallel [\bar{1}10])$, which is parallel to the wire direction [Fig. 5(a)]. It is also noteworthy that the first angular harmonics of the SO field Ω_1 in the $[110]$ wire are perpendicular to the wire direction ($\Omega_1 \perp [110]$) because of the strong lateral confinement. When $B_{\text{in}}(\vartheta)$ is rotated from $\vartheta = 90^\circ$ to $\vartheta = 180^\circ$, the spin-relaxation time is enhanced, as is indicated by the unchanging colored TRKR amplitude, which clearly remains at around 2 ns for $B_{\text{in}}(\vartheta = 180^\circ)$. On the other hand, the precession frequency is reduced for $B_{\text{in}}(\vartheta = 180^\circ)$ because the precession phase is shifted slightly towards a longer

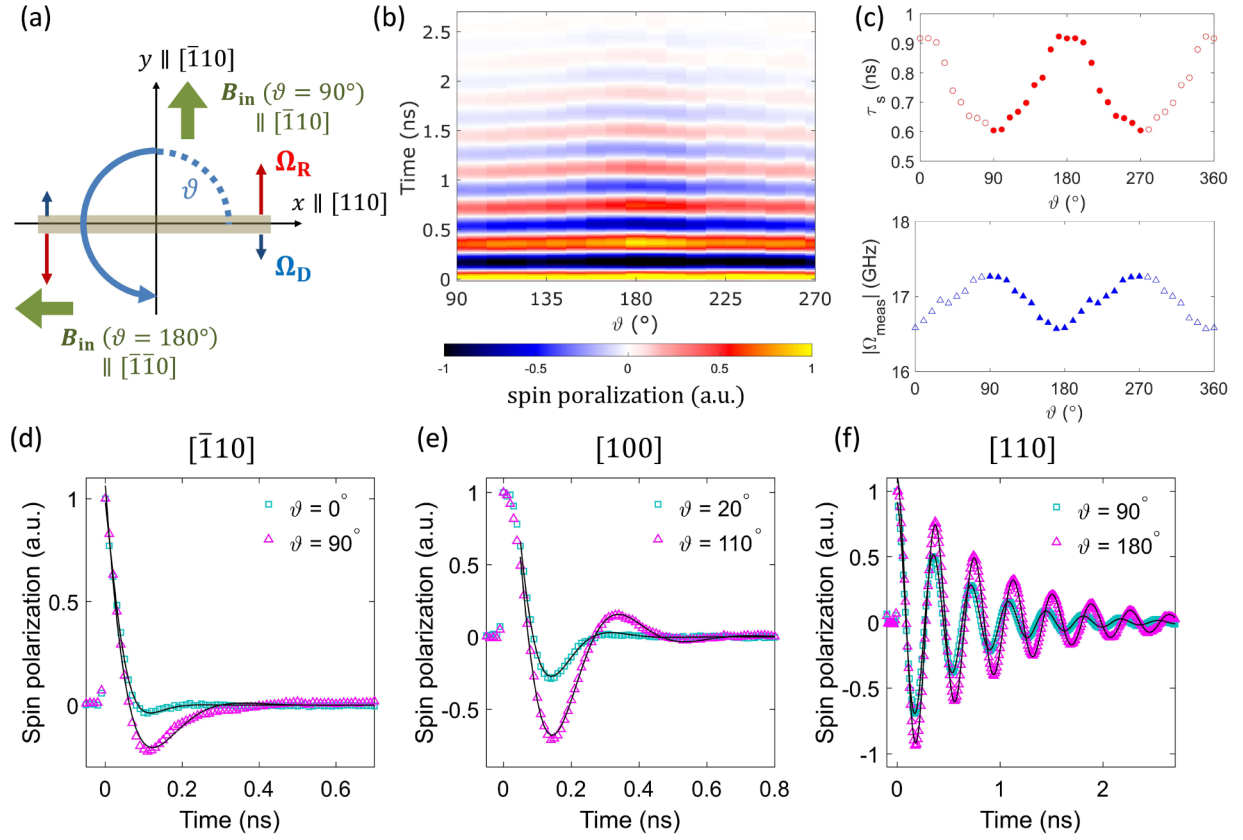


FIG. 5. Results of TRKR measurements in wire structures by applying the in-plane magnetic field $B_{\text{in}} = 0.65$ T at various $B_{\text{in}}(\vartheta)$ direction. Panel (a) represents the angle of the SO and external fields for the [110] wire. Panel (b) shows the color-coded plot of TRKR amplitude as functions of $B_{\text{in}}(\vartheta)$ directions and the delay time t for the [110] wire. Also, panel (c) shows the evaluated τ_s and $|\Omega_{\text{meas}}|$ fitting by Eq. (55). Panels (d)–(f) show the TRKR amplitude for the $[\bar{1}10]$, [100], and [110] wires where the $B_{\text{in}}(\vartheta)$ is parallel (blue circles) and perpendicular (red triangles) to the angle of the SO field.

delay time than that of the TRKR trace in $B_{\text{in}}(\vartheta = 90^\circ)$. The difference in the TRKR traces shown in Fig. 5(f) is clear evidence of the frequency modulation between the $B_{\text{in}}(\vartheta = 90^\circ)$ and $B_{\text{in}}(\vartheta = 180^\circ)$ angles. Particularly, these two conditions satisfy the developed analytical model in Eqs. (24) and (30), which correspond to the time evolution of the spin z component in an in-plane magnetic field parallel [$B_{\text{in}}(\vartheta = 90^\circ)$] and perpendicular [$B_{\text{in}}(\vartheta = 180^\circ)$] to the SO field, respectively. Here, because the third angular harmonic term Δ_3 is two orders of magnitude smaller than the Larmor frequency in the sample, we can explain the entire physics without considering the Δ_3 term. Based on Eqs. (24) and (30), two striking effects emerge in the spin-relaxation rate and precession frequency. For the magnetic field parallel to the SO field [$B_{\text{in}}(\vartheta = 90^\circ)$] where spin precession takes place in the x - z plane, the precession frequency is defined solely by the external magnetic field (ξ_{\parallel}) in Eq. (24). This is because the spin-relaxation rate for x (\parallel [110])- and z (\parallel [001])-oriented spins is the same due to lateral confinement. As a result, the spins along the x and z directions experience identical torques during precession, resulting in no spin-relaxation anisotropy. In such a case, the spin-relaxation rate is simply governed by the Δ_1 term, i.e., $\Omega_1 \perp$ [110], in Eq. (24). For the magnetic field perpendicular to the SO field [$B_{\text{in}}(\vartheta = 180^\circ)$], where spin precession occurs in the y - z plane [Fig. 5(a)], spin relaxation is suppressed for spin orientations along the y direction

parallel to Ω_1 . This results in anisotropic spin relaxation between y - and z -oriented spins. As a result, the spin-relaxation rate is reduced by a factor of 2 in Eq. (30). Such spin-relaxation anisotropy also reduces the precession frequency to ξ_{\perp} in Eq. (30). Similar modulation on the spin-relaxation rate and precession frequency is also observed in $[\bar{1}10]$ and [100] wires under a $B_{\text{in}}(\vartheta)$ field parallel and perpendicular to the SO field [Figs. 5(d) and 5(e)], clearly indicating the interaction between the SO and in-plane magnetic field directions. To elucidate the observed anisotropic spin dynamics in the wire, we used Eq. (55) to quantitatively evaluate τ_s and $|\Omega_{\text{meas}}|$ in various $B_{\text{in}}(\vartheta)$ directions. Representative fitting results are shown as the black curves in Figs. 5(d)–5(f). For the [110] wires, Fig. 5(c) summarizes all the extracted τ_s and $|\Omega_{\text{meas}}|$, indicated by the filled circles and triangles, respectively, as a function of the $B_{\text{in}}(\vartheta)$ direction. Because of the spatial symmetry of the measurement configurations, we safely extend the result to $0^\circ \leq \vartheta < 90^\circ$ and $270^\circ < \vartheta \leq 360^\circ$, as shown by the open symbols. Both τ_s and $|\Omega_{\text{meas}}|$ show oscillatory behavior with respect to the $B_{\text{in}}(\vartheta)$ direction. To further understand the spin-relaxation and frequency anisotropy in wires, we conducted the same analysis in other wires to extract τ_s and $|\Omega_{\text{meas}}|$ under various $B_{\text{in}}(\vartheta)$ direction and summarized the results for all $[\bar{1}10]$, [100], and [110] wires as polar plots in Figs. 6(a)–6(f). The blue solid lines are the fitted curves from Eqs. (48) and (52). All the wire orientations exhibit

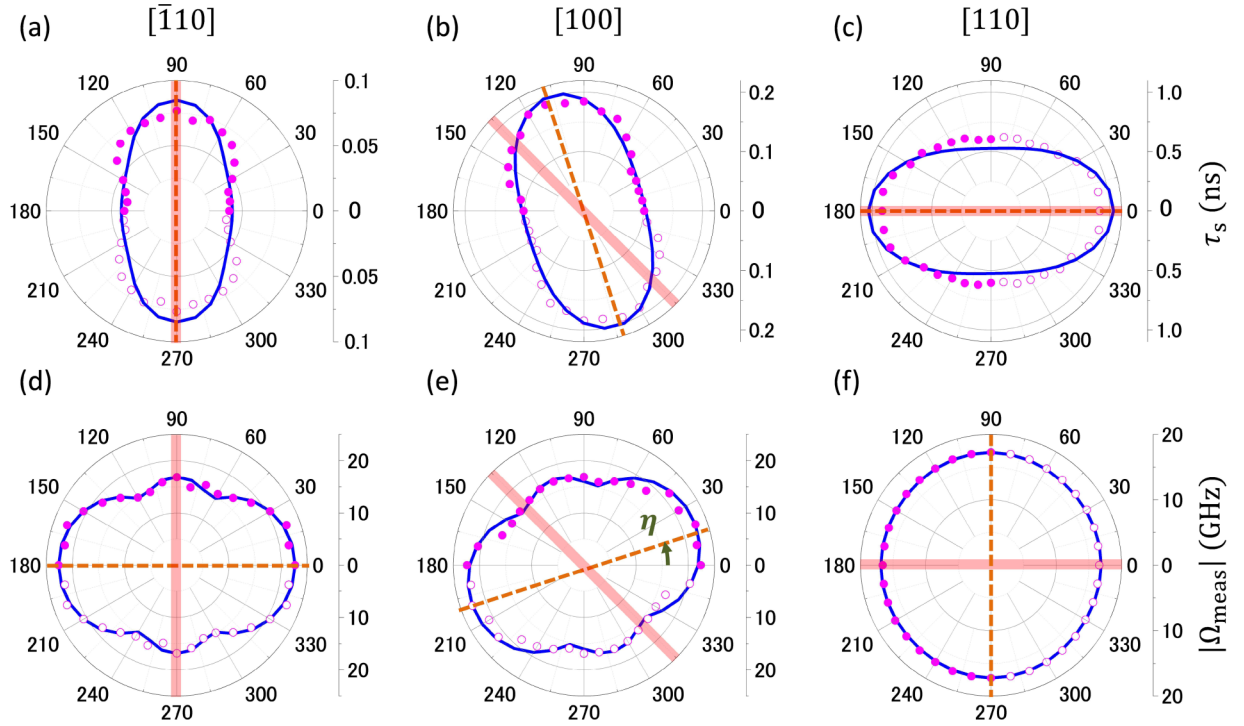


FIG. 6. The spin-relaxation time and the frequency anisotropy in $[\bar{1}10]$, $[100]$, and $[110]$ wires by applying the in-plane magnetic field $B_{\text{in}} = 0.65$ T at various $\mathbf{B}_{\text{in}}(\vartheta)$ direction. The blue solids are the fitted curves from Eqs. (48) and (52). The orange dashed line connects the maximum points. The red line corresponds to the wire orientations. The spin-relaxation time is approximately doubled when ϑ is perpendicular to the SO field. On the other hand, the precession frequency decreased when ϑ is perpendicular to the SO field.

anisotropy both for the spin-relaxation time [Figs. 6(a)–6(c)] and the precession frequency [Figs. 6(d)–6(f)], in which their amplitude and direction strongly depend on the wire orientation. For the $[\bar{1}10]$ and $[110]$ wires, the induced anisotropies on the spin relaxation and the precession frequency are parallel and perpendicular to the wire orientation, respectively. This orientation is understood because both the Rashba and Dresselhaus SO fields are parallel (antiparallel) to each other in the $[\bar{1}10]$ ($[110]$) crystal orientation, and the total SO field $\mathbf{\Omega}_1$ remains perpendicular to the wire orientation. Because of the additive contribution to the two SO fields in the $[\bar{1}10]$ wires, the τ_s value is smaller than that of the $[110]$ wires by a factor of 10. The spin-relaxation anisotropy defined by $\tau_s(\mathbf{B}_{\text{in}}(\vartheta) \perp \mathbf{\Omega}_1) / \tau_s(\mathbf{B}_{\text{in}}(\vartheta) \parallel \mathbf{\Omega}_1)$ was found to be 1.91 and 1.53 for the $[\bar{1}10]$ and $[110]$ wires, respectively. In Figs. 6(d) and 6(f), because the total SO field in the $[\bar{1}10]$ wires is larger than that in $[110]$ wires, the corresponding frequency anisotropy is also enhanced in the $[\bar{1}10]$ wires, where an additional kink structure is observed around $\mathbf{B}_{\text{in}}(\vartheta = 90^\circ)$ in Fig. 6(d). In the case of the $[100]$ wires, on the other hand, the induced anisotropy is tilted from the wire orientation even though the orthogonal anisotropy between spin relaxation and precession frequency is maintained. This tilt in anisotropy occurs because the Dresselhaus SO field is perpendicular to the Rashba SO field in the $[100]$ crystal orientation [Fig. 4(a)]. Consequently, the total SO field $\mathbf{\Omega}_1$ is tilted from the wire orientation. The ratio of $\tau_s(\mathbf{B}_{\text{in}}(\vartheta) \perp \mathbf{\Omega}_1) / \tau_s(\mathbf{B}_{\text{in}}(\vartheta) \parallel \mathbf{\Omega}_1)$ was 1.99 for the $[100]$ wire. These characteristic features in the TRKR measurements are in excellent agreement with the developed theory presented in Fig. 3. According to Eqs. (43) and (46),

the induced anisotropy is governed by the spin-relaxation rate Δ_1 .

For the quantitative evaluation of Δ_1 , i.e., the Rashba and Dresselhaus SO coefficients, we fit the τ_s and $|\Omega_{\text{meas}}|$ according to the theoretical description of effective τ_s and the Larmor frequency ν for arbitrary $\mathbf{B}_{\text{in}}(\vartheta)$ direction. It is noteworthy that we neglect Δ_3 for the fitting because Δ_3 is much smaller than Δ_1 in our sample. Because the Larmor frequency under $B_{\text{in}} = 0.65$ T is comparable to Δ_1 , we used Eqs. (48) and (52) to adopt moderately strong magnetic fields. The blue solid curves in Figs. 6(a)–6(f) show the fitting results for each wire orientation, and are in remarkably good agreement with the experimentally obtained results. The maximum and minimum τ_s differ by a factor of 2, as predicted from theory. This was reproduced in the experiments except in the case of the $[110]$ wire. This is because the SO field is small in the case of the $[110]$ wire, and the influence of the EY spin-relaxation mechanism is therefore relatively large. In both the experiments and the fitting for the $[\bar{1}10]$ and $[100]$ wires, the Larmor frequency shows the kink when the $\mathbf{B}_{\text{in}}(\vartheta)$ is parallel to the SO field direction. Similar behavior was also observed in the weak localization anisotropy in the wire. It can be explained by the partial symmetry recovery [41]. The evaluated Δ_1 values for the $[\bar{1}10]$, $[100]$, and $[110]$ wires and the corresponding theoretical values are presented in Table I. For the theoretical values, we used the SO coefficients obtained from spin-diffusion measurements in Fig. 4. The Δ_1 from Larmor frequency ν is in good agreement with the theoretical values, whereas the Δ_1 from effective τ_s fitting is larger than the theoretical values by a factor of 2 to 3. These findings

TABLE I. Δ_1 values for each wire evaluated from the SO field [Eq. (13)] and fitting in Fig. 6.

Wire direction	$[\bar{1}10]$	[100]	[110]
Theoretical value	45.43	26.39	7.29
Fitted Larmor frequency anisotropy (10^9 s $^{-1}$)	34.34	29.53	7.59
Fitted spin-relaxation time anisotropy (ns)	147.72	61.87	11.73

indicate the evaluated spin-relaxation times in the wires are smaller than we expected from the Rashba and Dresselhaus SO coefficients evaluated. It is possible that the reason for this discrepancy is that spin relaxation other than the DP mechanism contributes to the reduction of τ_s , such as diffusive scattering at the wire edge and/or the EY spin-relaxation mechanism near the wire edge. We have measured the wire-width dependence of spin-relaxation time for the [110] wire (not shown). As the wire width decreases from 15 to 1 μm , the spin-relaxation time is monotonously increased from 100 to 920 ps. Several theoretical models are proposed in wire-width dependence of spin-relaxation time by considering either the DP or the EY mechanism. In the case of the DP mechanism as the dominant contribution, in quasi-1D wires with a specular boundary, spin-relaxation time is increased with the wire width decreases, but is saturated by further decreases in the wire width since multiple specular scattering at the boundary does not contribute to suppressing the spin relaxation [42]. On the other hand, with a diffusive boundary, the spin-relaxation time is kept longer for narrower wire because the motion narrowing is effectively enhanced by the diffusive scattering at the wire edge [42]. The effect of the EY mechanism on narrow wires has been also investigated [36,37]. As the wire width is decreased, the spin-relaxation time decreases because of the more frequent boundary collisions, resulting in the enhancement of the EY mechanism. If the EY mechanism at the boundary dominantly takes place, the spin-relaxation time should decrease in narrower wires, which was not the case in our experimental results. This indicates that the EY mechanism at least partly contributes to the spin relaxation and a more systematic study will be necessary to clarify the EY mechanism in the wire structures. Another possible reason is that the mean free path is similar in length to the wire width, and these could be modifications to the spin-relaxation theory [43]. However, because the Larmor frequency is purely induced by the SO field and external magnetic field, it is less affected by other non-SO-related mechanisms. Consequently, we use Δ_1 obtained from the frequency anisotropy to evaluate the Rashba and Dresselhaus SO coefficients. Using the orthogonal relation between the Rashba and Dresselhaus SO fields along the [100] crystal orientation, we directly separate α and β_1 coefficients solely from the [100] wire. Given the similarity of the weak localization anisotropy [41,44,45], the $\mathbf{B}_{\text{in}}(\vartheta)$ direction at the largest Larmor frequency in the [100] wire is described as

$$\frac{\beta_1}{\alpha} = \tan(45^\circ - \eta). \quad (58)$$

The observed η in Fig. 6(e) is 18° with respect to the $x \parallel [110]$ axis, corresponding to $\beta_1/\alpha = 0.51$. Together with $\Delta_1(\phi = 45^\circ) = 2\tau(\sqrt{\alpha^2 + \beta_1^2} k_F/\hbar)^2 = 29.53 \times 10^9$ s $^{-1}$, we evaluate α and β_1 , respectively, as -3.28×10^{-13} and $-1.67 \times$

10^{-13} eV m. These values are in good agreement with the SO values obtained from the spin-diffusion measurements in Fig. 4, enabling us to make a precise evaluation of the SO coefficients in the wire structure.

VII. CONCLUSION

We have theoretically and experimentally investigated anisotropic spin dynamics in semiconductor narrow wires induced by the interaction between the spin-orbit field and the Larmor precession under an in-plane magnetic field. The developed theory describes the modulation of the spin-relaxation rate and the spin-precession frequency depending on the in-plane magnetic field angle with respect to the SO field direction. Depending on the spin-precessional plane determined by the in-plane magnetic field direction, the SO field induces spin-relaxation anisotropy or isotropy between perpendicular and in-plane spins to the in-plane magnetic field, resulting in a modulation of the precession frequency and the spin-relaxation rate. There is a twofold difference in the spin-relaxation rate depending on whether the magnetic field is applied parallel or perpendicular to the SO field direction. In addition, the predicted anisotropy in the spin-relaxation rate and the precession frequency are orthogonal. Using 800-nm-width wires along the $[\bar{1}10]$, [100], and [110] crystal orientations based on a GaAs/AlGaAs quantum well, we demonstrated the predicted anisotropy on both spin relaxation and precession frequency by time-resolved Kerr rotation microscopy at 30 K. For $[\bar{1}10]$ and [110] wires, because the Rashba and Dresselhaus SO fields are aligned in the same direction (perpendicular to the wire orientation), the spin-relaxation time is the longest (shortest) when the in-plane magnetic field is parallel (perpendicular) to the wire orientation. The precession frequency exhibits the opposite symmetry, where the frequency is reduced when the in-plane magnetic field is parallel to the wire orientation. In the case of the [100] wire, even though such anisotropic behaviors with respect to the SO field are also observed, the anisotropy is tilted from the wire orientation because the two SO fields are mutually orthogonal. All results are in good agreement with the developed theory. The Rashba and Dresselhaus SO coefficients obtained from the [100] wires are virtually identical to the values independently evaluated from the spin-diffusion measurements. This study paves the way to the precise control of the spin state and to the ability to accurately evaluate the SO coefficient in narrow wires, thereby providing important insights into quantum and topological information based on semiconductor 1D wires.

ACKNOWLEDGMENTS

M.Ka. and U.Z. were supported by the Marsden Fund from New Zealand government funding (Contract No. VUW1713),

managed by the Royal Society Te Apārangi. M.Ka. was further supported by the Center for Science and Innovation in Spintronics at Tohoku University, Japan. M.K. and J.N. are supported via a Grant-in-Aid for Scientific Research (Grant No. 21H04647) from the Japan Society for the Promotion of Science. This work was also supported by the JST FOREST Program (Grant No. JPMJFR203C). D.I. acknowledges financial support from the Graduate Program in Spintronics at Tohoku University.

APPENDIX: SPIN DIFFUSION WITH SPECULAR BOUNDARIES

1. Non-Abelian gauge field representation

In order to consider the boundary effects on spin diffusion, it is illuminating to realize that because of the first angular harmonics in the SO field $\mathbf{\Omega}_1$ in the spin-diffusion operator (9), the SO contributions can be interpreted as ramifications of a non-Abelian gauge field \mathbf{A} . The latter couples to the wave vector $\mathbf{q} \rightarrow \mathbf{q} + 2e\mathbf{A}/\hbar$ and allows the rewriting of Eq. (9) in a compact form [46], as

$$\Lambda(\mathbf{q}) = [\boldsymbol{\omega}]_{\times} - D_s \left[\mathbf{q} + \frac{2e}{\hbar} \mathbf{A}(\mathbf{\Omega}_1) \right]^2 - \hat{\tau}_{\text{DP}}^{-1}(\mathbf{\Omega}_3), \quad (\text{A1})$$

where a gauge field component parallel to an arbitrary unit vector $\hat{\mathbf{n}}$ reads as

$$A_n = \frac{2i\hbar^2\tau}{eD_s m^*} \langle k_n [\mathbf{\Omega}_1]_{\times} \rangle = \frac{i\hbar}{2ev_{\text{F}}} [\mathbf{\Omega}_1(\mathbf{k} = k_{\text{F}}\hat{\mathbf{n}})]_{\times}. \quad (\text{A2})$$

The second equality holds because $\langle k_n k_m \rangle = \delta_{nm} k_{\text{F}}^2/d$. When an electron diffuses along the direction $\hat{\mathbf{n}}$, the gauge field component A_n induces spin rotations about the vector $\mathbf{\Omega}_1(\mathbf{k} = k_{\text{F}}\hat{\mathbf{n}})$. Full rotation is performed if $2e\|A_n\|L_n/\hbar = 2\pi$, which defines the spin-precession length along $\hat{\mathbf{n}}$ as $L_n = 2\pi\|\mathbf{\Omega}_1(\mathbf{k} = k_{\text{F}}\hat{\mathbf{n}})\|/v_{\text{F}}$ and the associated wave vector $Q_n = 2\pi/L_n = v_{\text{F}}/\|\mathbf{\Omega}_1(\mathbf{k} = k_{\text{F}}\hat{\mathbf{n}})\|$ [47]. Matrix norm $\|A_n\|$ gives the maximum singular value of A_n . Moreover, because $\langle \mathbf{k} \epsilon_{nlm} \Omega_l \rangle^2 = \langle \Omega_n \Omega_m - \Omega^2 \delta_{nm} \rangle k_{\text{F}}^2/d$, the term $D_s(2e\mathbf{A}/\hbar)^2$ is equivalent to the DP tensor $\hat{\tau}_{\text{DP}}^{-1}$ with $\mathbf{\Omega} = \mathbf{\Omega}_1$. Therefore, the DP tensor in expression (A1) depends solely on the contribution of the third angular harmonic SO field $\mathbf{\Omega}_3$.

2. Spin-conserving specular boundary condition

To derive a spin-diffusion equation for narrow quantum wires of width W , we assume spin-reflecting walls perpendicular to the longitudinal direction of the wire, i.e., in an arbitrary transverse direction $\hat{\mathbf{u}} \perp \hat{\mathbf{z}}$ at $r_u = \pm W/2$. The walls constitute a barrier through which the spin-diffusion current cannot pass and therefore impose the following condition [19]:

$$0 = \hat{\mathbf{u}} \cdot \mathbf{j}^{\text{s}}(\mathbf{r}, t) \Big|_{r_u = \pm W/2} \quad (\text{A3})$$

for the spin-current density \mathbf{j}^{s} , with the tensorial components j_n^{sm} , where $n, m \in \{x, y, z\}$. In compliance with Eqs. (8) and (A1), the expression for a current-density vector

component $j_u^{\text{s}} = (j_u^{\text{s}_x}, j_u^{\text{s}_y}, j_u^{\text{s}_z})$ in real space in the direction of the boundaries (unit vector $\hat{\mathbf{u}}$) takes the form [19,34]

$$j_u^{\text{s}}(\mathbf{r}, t) = \frac{D_s}{i} \left(-i \frac{\partial}{\partial r_u} + \frac{2e}{\hbar} A_u \right) \mathbf{s}(\mathbf{r}, t). \quad (\text{A4})$$

By performing a non-Abelian gauge transformation $\mathbf{s} \rightarrow \mathbf{s}' = U_A \mathbf{s} U_A^{\dagger}$, where $U_A = \exp(i2eA_u r_u/\hbar)$, the equation simplifies to the Neumann boundary condition as

$$\frac{\partial \mathbf{s}'(\mathbf{r}, t)}{\partial r_u} = 0. \quad (\text{A5})$$

An infinite orthonormal basis set of transverse spin-density modes that satisfy this equation is $\{1/\sqrt{W}, \sqrt{2}/\sqrt{W} \cos[n\pi(r_u/W - 1/2)]\}$ with $n \in \mathbb{N}^+$ [34].

3. Spin diffusion in narrow wires

In mesoscopic wires, where widths W are smaller than the dephasing lengths l_{ϕ} (mean free path between inelastic scattering events), the diffusion is dominated by the lowest diffusion mode $\langle r_u | 0 \rangle \equiv 1/\sqrt{W}$, called a zero mode, which is a constant function along $\hat{\mathbf{u}}$ in the gauge-transformed system [cf. Eq. (A5)]. Projecting the spin-diffusion operator (A1) on the zero mode, i.e., $\Lambda_0(\mathbf{q}) := \langle 0 | U_A \Lambda(\mathbf{q}) U_A^{\dagger} | 0 \rangle$, is known as the zero-mode or the 1D-diffusive approximation because the diffusion becomes one-dimensional. By applying the gauge transformation together with the zero-mode approximation, the consequences are as follows: (i) it removes the u th component of the kinetic momentum (first term on the right-hand side) in Eq. (A1) because $\langle 0 | U_A (q_u + 2eA_u/\hbar) U_A^{\dagger} | 0 \rangle = 0$; and (ii) it yields corrections proportional to $WQ_u = Wv_{\text{F}}/\|\mathbf{\Omega}_1(\mathbf{k} = k_{\text{F}}\hat{\mathbf{u}})\|$ because $U_A = \mathbb{1} + O(WQ_u)$. For narrow wires, where the spin-precession length L_u is much greater than the wire width W , i.e., $WQ_u \ll 1$, the spin relaxation severely slows for certain spin textures [19,21,34,48–50]. In leading order, one can neglect the corrections $O(WQ_u)$ and the spin decoherence associated with the first harmonic SO field for wave vectors along $\hat{\mathbf{u}}$, i.e., $\mathbf{\Omega}_1(\mathbf{k} = k_{\text{F}}\hat{\mathbf{u}})$, disappears completely. In this limit, the spin-diffusion operator is equivalent to Eqs. (9) and (A1) when setting $q_u \rightarrow 0$ and $A_u \rightarrow 0$ [or equivalently $\mathbf{\Omega}_1(\mathbf{k}) \rightarrow \mathbf{\Omega}_1(k_u = 0)$], i.e., we obtain

$$\Lambda_0(\mathbf{q}) \approx [\boldsymbol{\omega}]_{\times} - D_s \left[\mathbf{q} + \frac{2e}{\hbar} \mathbf{A}(\mathbf{\Omega}_1) \right]_{q_u=A_u=0}^2 - \hat{\tau}_{\text{DP}}^{-1}(\mathbf{\Omega}_3). \quad (\text{A6})$$

The resulting expression resembles the spin-diffusion operator for a 1D-confined system, where the boundary engenders subband quantization and only the lowest subband is occupied. In such a scenario, the contribution of $\mathbf{\Omega}_1$ for wave vectors parallel to $\hat{\mathbf{u}}$ also vanishes. However, two crucial differences exist in Eq. (A6): (i) Because the averaging $\langle \cdot \rangle$ is performed over the 2D Fermi sphere, the diffusion constant differs by a factor 2 from the 1D case. (ii) In a 1D-confined system, the k -cubic SO terms would also be subject to size quantization, but such is not the case in the 1D-diffusive wires. Moreover, the DP tensor in Eq. (A6), involving the third angular harmonics $\mathbf{\Omega}_3$, remains that of a 2D-diffusive system.

- [1] K. J. Thomas, J. T. Nicholls, M. Y. Simmons, M. Pepper, D. R. Mace, and D. A. Ritchie, *Phys. Rev. Lett.* **77**, 135 (1996).
- [2] R. M. Potok, J. A. Folk, C. M. Marcus, and V. Umansky, *Phys. Rev. Lett.* **89**, 266602 (2002).
- [3] J. Schliemann, J. C. Egues, and D. Loss, *Phys. Rev. Lett.* **90**, 146801 (2003).
- [4] B. A. Bernevig, J. Orenstein, and S.-C. Zhang, *Phys. Rev. Lett.* **97**, 236601 (2006).
- [5] J. D. Koralek, C. P. Weber, J. Orenstein, B. A. Bernevig, S.-C. Zhang, S. Mack, and D. D. Awschalom, *Nature (London)* **458**, 610 (2009).
- [6] M. P. Walser, C. Reichl, W. Wegscheider, and G. Salis, *Nat. Phys.* **8**, 757 (2012).
- [7] M. Kohda, V. Lechner, Y. Kunihashi, T. Dollinger, P. Olbrich, C. Schönhuber, I. Caspers, V. V. Bel'kov, L. E. Golub, D. Weiss, K. Richter, J. Nitta, and S. D. Ganichev, *Phys. Rev. B* **86**, 081306(R) (2012).
- [8] C. P. Scheller, T.-M. Liu, G. Barak, A. Yacoby, L. N. Pfeiffer, K. W. West, and D. M. Zumbühl, *Phys. Rev. Lett.* **112**, 066801 (2014).
- [9] Y. Oreg, G. Refael, and F. von Oppen, *Phys. Rev. Lett.* **105**, 177002 (2010).
- [10] R. M. Lutchyn, J. D. Sau, and S. Das Sarma, *Phys. Rev. Lett.* **105**, 077001 (2010).
- [11] Y. Oreg, E. Sela, and A. Stern, *Phys. Rev. B* **89**, 115402 (2014).
- [12] S. Tomonaga, *Prog. Theor. Phys.* **5**, 544 (1950).
- [13] J. M. Luttinger and J. Math, *J. Math. Phys.* **4**, 1154 (1963).
- [14] O. M. Auslaender, H. Steinberg, A. Yacoby, Y. Tserkovnyak, B. I. Halperin, K. W. Baldwin, L. N. Pfeiffer, and K. W. West, *Science* **308**, 88 (2005).
- [15] Y. Jompol, C. J. B. Ford, J. P. Griffiths, I. Farrer, G. A. C. Jones, D. Anderson, D. A. Ritchie, T. W. Silk, and A. J. Schofield, *Science* **325**, 597 (2009).
- [16] M. I. D'yakonov and V. I. Perel', *Fiz. Tverd. Tela* **13**, 3581 (1971) [*Sov. Phys. Solid State* **13**, 3023 (1972)].
- [17] C. H. L. Quay, T. L. Hughes, J. A. Sulpizio, L. N. Pfeiffer, K. W. Baldwin, K. W. West, D. Goldhaber-Gordon, and R. D. Picciotto, *Nat. Phys.* **6**, 336 (2010).
- [18] S. Heedt, N. Traverso Ziani, F. Crépin, W. Prost, S. Trellenkamp, J. Schubert, D. Grützmacher, B. Trauzettel, and T. Schäpers, *Nat. Phys.* **13**, 563 (2017).
- [19] A. G. Mal'shukov and K. A. Chao, *Phys. Rev. B* **61**, R2413 (2000).
- [20] A. A. Kiselev and K. W. Kim, *Phys. Rev. B* **61**, 13115 (2000).
- [21] S. Kettemann, *Phys. Rev. Lett.* **98**, 176808 (2007).
- [22] Th. Schäpers, V. A. Guzenko, M. G. Pala, U. Zülicke, M. Governale, J. Knobbe, and H. Hardtdegen, *Phys. Rev. B* **74**, 081301(R) (2006).
- [23] A. W. Holleitner, V. Sih, R. C. Myers, A. C. Gossard, and D. D. Awschalom, *Phys. Rev. Lett.* **97**, 036805 (2006).
- [24] S. Z. Denega, T. Last, J. Liu, A. Slachter, P. J. Rizo, P. H. M. van Loosdrecht, B. J. van Wees, D. Reuter, A. D. Wieck, and C. H. van der Wal, *Phys. Rev. B* **81**, 153302 (2010).
- [25] J. Ishihara, M. Ono, Y. Ohno, and H. Ohno, *Appl. Phys. Lett.* **102**, 212402 (2013).
- [26] P. Altmann, M. P. Walser, C. Reichl, W. Wegscheider, and G. Salis, *Phys. Rev. B* **90**, 201306(R) (2014).
- [27] P. Altmann, M. Kohda, C. Reichl, W. Wegscheider, and G. Salis, *Phys. Rev. B* **92**, 235304 (2015).
- [28] J. Ishihara, Y. Ohno, and H. Ohno, *Appl. Phys. Express* **7**, 013001 (2014).
- [29] A. V. Larionov and L. E. Golub, *Phys. Rev. B* **78**, 033302 (2008).
- [30] D. J. English, J. Hübner, P. S. Eldridge, D. Taylor, M. Henini, R. T. Harley, and M. Oestreich, *Phys. Rev. B* **87**, 075304 (2013).
- [31] M. Kammermeier, P. Wenk, and J. Schliemann, *Phys. Rev. Lett.* **117**, 236801 (2016).
- [32] D. Iizasa, M. Kohda, U. Zülicke, J. Nitta, and M. Kammermeier, *Phys. Rev. B* **101**, 245417 (2020).
- [33] R. Winkler, *Spin-Orbit Coupling Effects in Two-Dimensional Electron and Hole Systems*, Springer Tracts in Modern Physics Vol. 191 (Springer-Verlag, Berlin, 2003).
- [34] P. Wenk and S. Kettemann, *Phys. Rev. B* **81**, 125309 (2010).
- [35] P. Wenk and S. Kettemann, Spin relaxation in quantum wires, in *Handbook on Nanophysics*, edited by K. Sattler (Taylor & Francis, Boca Raton, 2010), p. 49.
- [36] P. Schwab, M. Dzierzawa, C. Gorini, and R. Raimondi, *Phys. Rev. B* **74**, 155316 (2006).
- [37] J. Tsai and C.-H. Chang, *J. Phys.: Condens. Matter* **24**, 075801 (2012).
- [38] G. Salis, D. D. Awschalom, Y. Ohno, and H. Ohno, *Phys. Rev. B* **64**, 195304 (2001).
- [39] M. Kohda, P. Altmann, D. Schuh, S. D. Ganichev, W. Wegscheider, and G. Salis, *Appl. Phys. Lett.* **107**, 172402 (2015).
- [40] D. Iizasa, A. Aoki, T. Saito, J. Nitta, G. Salis, and M. Kohda, *Phys. Rev. B* **103**, 024427 (2021).
- [41] A. Sasaki, S. Nonaka, Y. Kunihashi, M. Kohda, T. Bauernfeind, T. Dollinger, K. Richter, and J. Nitta, *Nat. Nanotechnol.* **9**, 703 (2014).
- [42] Y. Kunihashi, M. Kohda, and J. Nitta, *Phys. Rev. B* **85**, 035321 (2012).
- [43] E. Khalaf and P. M. Ostrovsky, *Phys. Rev. B* **94**, 165431 (2016).
- [44] M. Scheid, M. Kohda, Y. Kunihashi, K. Richter, and J. Nitta, *Phys. Rev. Lett.* **101**, 266401 (2008).
- [45] T. Nishimura, K. Yoshizumi, T. Saito, D. Iizasa, J. Nitta, and M. Kohda, *Phys. Rev. B* **103**, 094412 (2021).
- [46] We consider here a charge $2e$ as a reminder of the relation of the spin-diffusion equation to the diffuson and cooperon propagators in quantum transport, which represent two-particle quantum interference corrections (as described in [34,51]).
- [47] Matrix norm $\|A_n\|$ gives the maximum singular value of A_n .
- [48] P. Wenk and S. Kettemann, *Phys. Rev. B* **83**, 115301 (2011).
- [49] M. Kammermeier, P. Wenk, J. Schliemann, S. Heedt, T. Gerster, and T. Schäpers, *Phys. Rev. B* **96**, 235302 (2017).
- [50] M. Kammermeier, P. Wenk, F. Dirnberger, D. Bougeard, and J. Schliemann, *Phys. Rev. B* **98**, 035407 (2018).
- [51] J. Rammer, *Quantum Transport Theory* (Westview Press, Boulder, 2004).